Delft University of Technology

Document Version
Final published version

Licence
Dutch Copyright Act (Article 25fa)

Citation (APA)
Yan, X., Du, L., Yang, Z., Du, W., Tian, T., Wang, X., Li, W., Zhang, G., & Fan, J. (2026). Confocal Raman spectroscopy-based evaluation of interfacial residual stresses and warpage in power electronics packaging with sintered copper nanoparticle interconnects. *Applied Thermal Engineering*, *282*, Article 128796. https://doi.org/10.1016/j.applthermaleng.2025.128796

Important note
To cite this publication, please use the final published version (if applicable).
Please check the document version above.

Copyright
In case the licence states “Dutch Copyright Act (Article 25fa)”, this publication was made available Green Open Access via the TU Delft Institutional Repository pursuant to Dutch Copyright Act (Article 25fa, the Taverne amendment). This provision does not affect copyright ownership.
Unless copyright is transferred by contract or statute, it remains with the copyright holder.

Sharing and reuse
Other than for strictly personal use, it is not permitted to download, forward or distribute the text or part of it, without the consent of the author(s) and/or copyright holder(s), unless the work is under an open content license such as Creative Commons.

Takedown policy
Please contact us and provide details if you believe this document breaches copyrights.
We will remove access to the work immediately and investigate your claim.

This work is downloaded from Delft University of Technology.

Green Open Access added to TU Delft Institutional Repository
as part of the Taverne amendment.

More information about this copyright law amendment
can be found at https://www.openaccess.nl.

Otherwise as indicated in the copyright section:
the publisher is the copyright holder of this work and the
author uses the Dutch legislation to make this work public.

Applied Thermal Engineering 282 (2026) 128796

Contents lists available at ScienceDirect

Applied Thermal Engineering

journal homepage: www.elsevier.com/locate/apthermeng

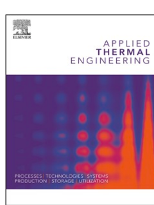

Research Paper

Confocal Raman spectroscopy-based evaluation of interfacial residual stresses and warpage in power electronics packaging with sintered copper nanoparticle interconnects

Xuyang Yan [a], Leiming Du [b], Zhoudong Yang [a], Wei Du [a], Tiancheng Tian [a], Xueliang Wang [a], Wenyu Li [a], Guoqi Zhang [b], Jiajie Fan [a,b,c,*]

[a] *Shanghai Engineering Technology Research Center of SiC Power Device, College of Intelligent Robotics and Advanced Manufacturing, Fudan University, Shanghai 200433, China*
[b] *EEMCS Faculty, Delft University of Technology, Delft 2628CD, the Netherlands*
[c] *Research Institute of Fudan University in Ningbo, Ningbo 315327, China*

ARTICLE INFO

Keywords:
Confocal Raman spectroscopy
Sintered Cu nanoparticles
Residual stress
Thermal-induced warpage
Thermo-mechanical model

ABSTRACT

Residual stress and thermally induced warpage are critical reliability concerns in power electronic packaging, particularly when employing sintered copper nanoparticle (Cu NP) interconnects. While these interconnects provide high thermal and electrical performance, they also introduce significant interfacial stresses during bonding that alter mechanical behavior during service. This study develops an integrated confocal Raman–analytical modeling framework to directly quantify and mechanistically interpret these stresses in a representative SiC/Sintered Cu NPs/Active Metal Brazing ceramic substrate (AMB) stack. Raman spectroscopy reveals a compressive interfacial stress field peaking at −334 MPa near the chip center with localized hotspots linked to microporosity. Complementary in-situ Moiré interferometry tracked warpage evolution during thermal cycle (30–310°C). Coupling this stress measurement with a three-dimensional thermoelastic model, and explicitly assigning the bonding temperature as the stress-free reference, enables accurate reproduction of the temperature-dependent warpage trajectory. The model predictions align with experimental interferometry within $<$ 5% deviation. These results demonstrate that incorporating residual stress is essential to realistically capture thermo-mechanical evolution. The proposed Raman–model paradigm advances beyond prior purely numerical or purely experimental efforts by bridging quantitative stress mapping with predictive warpage modeling. This methodology provides essential insights for thermal-induced residual stress and warpage managements in high-temperature power electronics packaging, providing a stress-informed foundation for reliability assessment and design optimization.

1. Introduction

With the rapid development of renewable energy, electric transportation, and high-frequency power systems, power chip packaging architectures are increasingly exposed to higher current densities, elevated thermal loads, and demanding service environments [1,2]. To achieve high-throughput bonding and meet the reliability demands of high-temperature operation, pressure-assisted sintering has emerged as a widely studied solution for die-attach materials. Silver (Ag) nanoparticles (NPs) [3,4], owing to their excellent electrical and thermal properties, have already been deployed in the power electronic packaging. In comparison, copper (Cu) NPs [5,6] offer substantial advantages in cost-effectiveness and process compatibility, making them a promising alternative of Ag sintering for high-temperature bonding of wide-bandgap devices such as silicon carbide (SiC) [7]. Sintering processes typically involve high temperatures and applied pressure, which can readily introduce non-uniform residual stresses at the chip–substrate interface [8]. These residual stresses can significantly affect the mechanical response of the packaging structure under cyclic thermal loads [9]. Accurate assessment of the residual stresses induced during the

* Corresponding author at: Shanghai Engineering Technology Research Center of SiC Power Device, College of Intelligent Robotics and Advanced Manufacturing, Fudan University, Shanghai 200433, China.
E-mail address: jiajie_fan@fudan.edu.cn (J. Fan).

https://doi.org/10.1016/j.applthermaleng.2025.128796
Received 22 June 2025; Received in revised form 24 September 2025; Accepted 20 October 2025
Available online 23 October 2025
1359-4311/© 2025 Elsevier Ltd. All rights reserved, including those for text and data mining, AI training, and similar technologies.

nanoparticle sintering process is essential for reliable lifetime prediction and mechanical integrity evaluation of power electronic devices [10,11]. In actual operation, long-term cyclic thermal loads can further intensify thermally induced warpage and the evolution of dynamic stresses [12]. However, due to limitations in characterization techniques and cost constraints, this critical physical factor is often underestimated or overlooked in reliability design. Therefore, precise evaluation of residual stress distribution and a deeper understanding of its formation mechanism are not only fundamental to advancing reliability research in electronic packaging, but also essential for achieving robust packaging design in industrial applications.

Many previous studies have focused on simulation and analytical models to evaluate the thermo-mechanical behavior of electronic packaging. Finite element analysis (FEA) has long served as the predominant method for modeling the thermo-mechanical behavior of electronic packaging structures [13,14]. It is extensively employed for predicting stress distributions and warpage across multilayer heterogeneous systems. Wong et al. [15] conducted a detailed FEA-based study on the stress response and warpage of redistribution layers under thermal loading in power modules, validating the efficacy of FEA in interlayer stress characterization. Discrete element analysis (DEA) has also been employed to predict mechanical stresses within the microstructures of electronic components [16]. However, FEA and DEA suffer from high computational costs and limited spatial resolution in capturing interfacial stress gradients, particularly across material boundaries. Analytical modeling, on the other hand, offers lower computational burden and has been explored for multi-layered composite structures [17–19]. Existing analytical models are mostly derived from simplified tri-layer assumptions [20], thermal expansion mismatch theory [21], or Suhir-based solutions [22], and are generally limited to specific boundary conditions or uniaxial thermal gradients, making them difficult to extend to complex multilayer packaging systems. Wang et al. [23] employed a theoretical thermoelastic model to predict warpage in large-scale laminated packaging structures. However, both existing analytical and numerical frameworks typically neglect the influence of residual stresses generated during the packaging process, which introduces notable discrepancies in subsequent predictions of device behavior. These limitations underscore the need for a mathematically rigorous and computationally efficient predictive framework that explicitly incorporates residual stress effects in multilayer electronic packaging systems.

While prior advances in theoretical modeling and FEA have provided valuable insights into the thermo-mechanical behavior of multilayer packaging structures, the omission of residual stress—a critical consequence of manufacturing processes—continues to undermine the accuracy of stress predictions and long-term reliability assessments. Addressing this gap calls for high-resolution experimental techniques capable of capturing interfacial stress fields with precision. Conventional techniques for residual stress analysis, such as XRD [24,25], ultrasonic methods [26,27], EBSD [28], and optical interferometry [27], suffer from limited penetration depth, surface-only applicability, or destructiveness, making them unsuitable for accurate, efficient, and non-destructive evaluation of interfacial stress in SiC chip packaging. Synchrotron radiation [29] and neutron diffraction [30,31] offer high-precision residual stress measurement, but their high costs and dimensional limitations restrict widespread application. In contrast, confocal Raman spectroscopy [32–34], an emerging stress testing method, offers significant advantages. This technique analyzes the frequency shift of Raman scattered light within materials to non-destructively measure residual stress in small regions, providing high-precision information on stress distribution at both surface and sub-surface levels [32]. Its unique spatial resolution allows for the precise measurement of stress distribution at different material interfaces in SiC packaging [35]. Yang et al. [36] proposed a temperature-dependent Raman stress prediction model, which incorporates a thermal correction factor and temperature-variable elastic modulus to enable high-precision, non-destructive evaluation of temperature-induced stresses in 4H-SiC. As such, a confocal Raman-based, non-destructive methodology holds strong promise for capturing in-plane residual stress distributions and guiding the refinement of thermo-mechanical models in chip-to-substrate architectures.

In summary, this study explicitly integrates confocal-Raman–derived interfacial stress fields into a Fourier-based thermo-mechanical warpage model and validate it by in-situ Moiré interferometry under thermal cycling for sintered Cu NP packaging. By focusing on the representative SiC/Sintered Cu NPs/Active Metal Brazing ceramic substrate (AMB) stack, it elucidates the critical role of sintering-induced residual stress and demonstrates the unique advantages of confocal Raman spectroscopy for packaging-level stress characterization. The proposed framework offers a rigorous foundation for predictive modeling and process-informed design of next-generation high-reliability power modules.

2. Methodology

2.1. Sample preparation

Fig. 1 illustrates the preparation protocol for pressure-assisted sintered Cu NP specimens. A Cu NP slurry, synthesized based on a previously reported method [37], was thoroughly homogenized to ensure uniform particle dispersion and prevent local agglomeration, which is critical for achieving consistent bonding performance. The slurry contained Cu NPs with an average particle size of approximately 200 nm, providing a high surface area and enhanced sinterability. An automatic screen-printing system (EKRA Serio 400, Automatisierungssysteme GmbH) was employed to uniformly apply the homogenized slurry onto an AMB substrate. A custom stainless-steel screen with a mesh thickness of 100 μm was used. Key screen printing parameters included a squeegee pressure of 30 MPa, printing speed of 30 mm/s, and release speed of 10 mm/s, ensuring uniform thickness and good edge definition of the Cu NP layer. After deposition, the printed samples were dried in a nitrogen atmosphere at 120 °C for 5 mins to remove solvents and promote layer stability. A 10 mm × 10 mm 4H- SiC chip was subsequently aligned and mounted onto the dried Cu NP layer using an automatic pick-and-place system. The assembly was then subjected to pressure-assisted sintering using a Boschman Sinterstar Auto-F-XL-HC system. Sintering was carried out at 250 °C under a nitrogen atmosphere with an applied uniaxial pressure of 20 MPa for 3 mins. Upon completion, the samples were cooled to room temperature on a controlled cooling platform. As a result, the SiC chip was effectively bonded to the AMB substrate through the sintered Cu NP interlayer, forming a mechanically robust and thermally conductive interface suitable for high-reliability power electronics applications.

2.2. Thermomechanical analytical modeling

To analytically evaluate the thermo-mechanical behavior of the multilayer SiC/Sintered Cu NPs/AMB stack, a closed-form solution was derived based on thermoelasticity theory and Fourier series expansion. The structure is simplified as a multilayered rectangular composite plate subject to in-plane constraints and uniform thermal loading. This study assumes that the three-dimensional packaging laminated plate has p layers, as depicted in Fig. 2(a). The primary analysis was conducted on the packaging laminated plate with length a, width b, thickness $h^{(i)}$ for each layer ($i = 1, 2, \ldots, p$), and total height H. In the working environment, because of factors such as chip power dissipation and ambient temperature variations—which cause overall temperature changes in the module—the laminated packaging plate is affected by temperature changes in the packaging module. In this study, the top and bottom surface temperatures of the laminated packaging plate were set to $T_t(x, y)$ and $T_b(x, y)$, respectively. When subjected to thermal loading, the bottom surface of the laminated plate was also under the action of a continuously distributed mechanical load $q(x, y)$ because of the effects

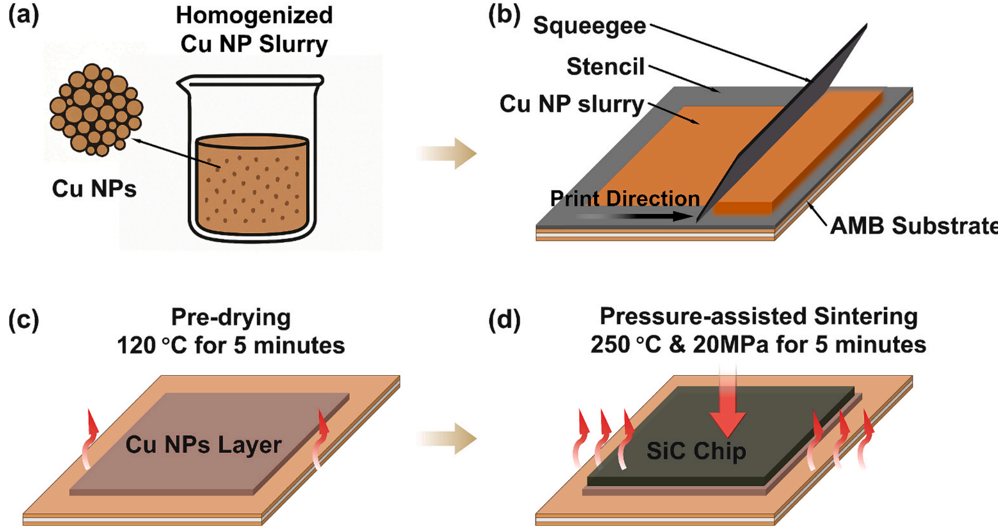

Fig. 1. Preparation process of pressure-assisted sintered Cu samples: (a) Cu NP slurry; (b) Stencil printing; (c) Pre-drying (120 °C, 5 mins); (d) Sintering (250 °C, 20 MPa, 3 mins).

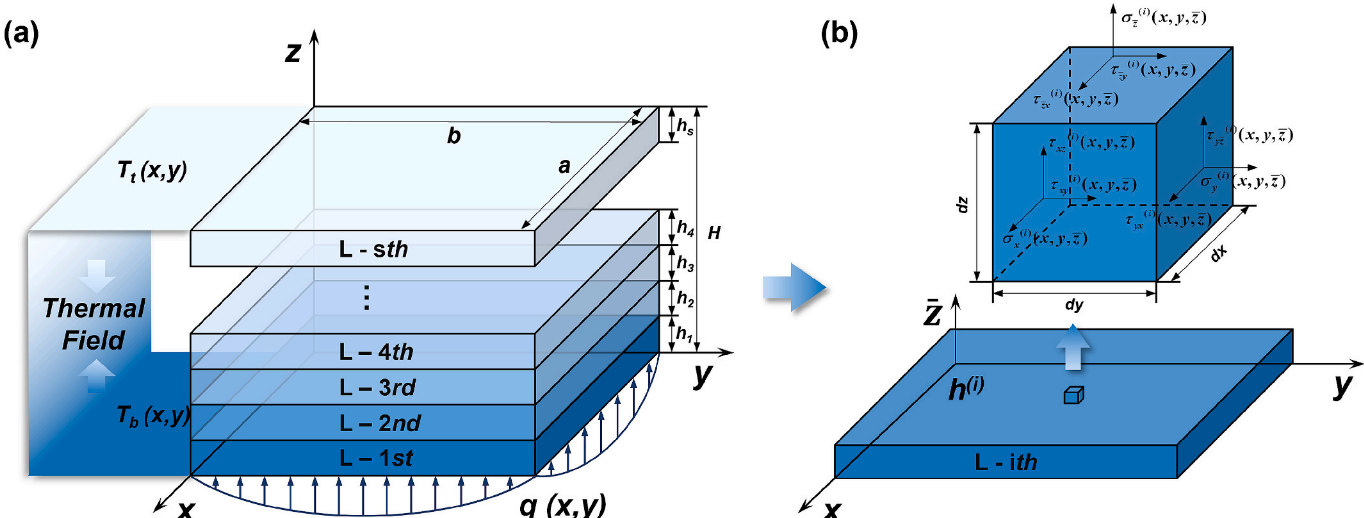

Fig. 2. Schematic of the thermo-mechanical theoretical model: (a) Geometric configuration of the multilayer stack; (b) Local coordinate system and definition of stress–strain components in the ith layer.

of gravity and residual stresses from the packaging. To analyze the mechanical properties of the i-th layer structure with uniform thickness $h^{(i)}$, a local Cartesian coordinate system was established for the study, as depicted in Fig. 2(b). The axes representing the length and width are denoted as x and y, respectively, and the axis representing the thickness or height is denoted as $z^{(i)}$. In the structural material properties of the i-th layer, the elastic modulus is represented by $E^{(i)}$, Poisson's ratio is represented by $\mu^{(i)}$, the CTE is represented by $\alpha^{(i)}$, and the thermal conductivity is represented by $k^{(i)}$.

To capture the temperature distribution across the plate under ambient variations, the steady-state three-dimensional heat conduction equation is employed:

$$\frac{\partial^2 T^{(i)}(x,y,\bar{z})}{\partial x^2}+\frac{\partial^2 T^{(i)}(x,y,\bar{z})}{\partial y^2}+\frac{\partial^2 T^{(i)}(x,y,\bar{z})}{\partial \bar{z}^2}=0 \tag{1}$$

To satisfy the prescribed adiabatic lateral surfaces and known top–bottom surface temperatures, the temperature field is expanded as a two-dimensional Fourier sine series:

$$T^{(i)}(x,y,\bar{z})=\sum_{m=1}^{\infty}\sum_{n=1}^{\infty}\frac{n\pi}{b}\left[e^{\beta_{mn}\bar{z}}\quad e^{-\beta_{mn}\bar{z}}\right]\left[\boldsymbol{XH}_{mn}^{(i)}\right]_{2\times 1}\sin\frac{m\pi x}{a}\sin\frac{n\pi y}{b} \tag{2}$$

The coefficient functions $T^{(i)}(x,y,\bar{z})$ are solved via ODEs derived from substituting the series into the heat equation. The resulting field is then cast into a matrix form to unify the expressions for temperature and vertical heat flux:

$$\begin{bmatrix} T^{(i)}(x,y,\bar{z}) \\ k^{(i)}\dfrac{\partial T^{(i)}(x,y,\bar{z})}{\partial \bar{z}} \end{bmatrix}=\sum_{m=1}^{\infty}\sum_{n=1}^{\infty}\begin{bmatrix} \dfrac{n\pi}{b}e^{\beta_{mn}\bar{z}} & \dfrac{n\pi}{b}e^{-\beta_{mn}\bar{z}} \\ k^{(i)}\dfrac{n\pi}{b}\beta_{mn}e^{\alpha_{mn}\bar{z}} & -k^{(i)}\dfrac{n\pi}{b}\beta_{mn}e^{-\alpha_{mn}\bar{z}} \end{bmatrix} \boldsymbol{XH}_{mn}^{(i)}\sin\frac{m\pi x}{a}\sin\frac{n\pi y}{b} \tag{3}$$

Next, by considering $\bar{z}$ to be 0 and $h^{(i)}$ in Eq. (5) and eliminating the coefficient matrix in the formula, the relationship between the temperature and heat flow on the upper and lower surfaces of the i-th layer structure can be derived. The temperature and heat flow at the adjacent contact interfaces of the laminated plate are equal, that is, $K_{mn}^{(i)}\left(h^{(i)}\right)=$

$K_{mn}^{(i+1)}(0)$. Layer-to-layer thermal continuity is enforced by matching interface heat flux and temperature, leading to a recursive matrix transmission formulation:

$$\boldsymbol{XH}_{mn}^{(i)} = \boldsymbol{C}_{mn}^{(i)}\left(h^{(i)}\right)^{-1}\left\{\prod_{j=i}^{1}\boldsymbol{C}_{mn}^{(j)}\left(h^{(j)}\right)\boldsymbol{C}_{mn}^{(j)}(0)^{-1}\right\}\boldsymbol{C}_{mn}^{(1)}(0)\boldsymbol{XH}_{mn}^{(1)} \tag{4}$$

The temperature boundary conditions for the upper and lower surfaces of the laminated plate can be represented as a Fourier series as follows:

$$\begin{cases} T^{(1)}(x,y,0) = \sum_{m=1}^{\infty}\sum_{n=1}^{\infty}\frac{4}{ab}\int_0^a\int_0^b t_1(x,y)\sin\frac{m\pi x}{a}\sin\frac{n\pi y}{b}dydx = t_1(x,y), \\ T^{(p)}(x,y,h^{(p)}) = \sum_{m=1}^{\infty}\sum_{n=1}^{\infty}\frac{4}{ab}\int_0^a\int_0^b t_2(x,y)\sin\frac{m\pi x}{a}\sin\frac{n\pi y}{b}dydx = t_2(x,y) \end{cases} \tag{5}$$

Here $T^{(1)}(x,y,0)$ represents the temperature distribution at the lower boundary of the first layer structure of the laminated plate, and $T^{(p)}(x,y,h^{(p)})$ represents the temperature distribution at the upper boundary of the p-th layer (top layer) structure of the laminated plate. When $i = p$, combining Eq. (5) with Eq. (6) allows for the solution of the coefficient matrices $XH_{mn}^{(1)}$ and $XH_{mn}^{(p)}$. Subsequently, by substituting coefficient matrix $XH_{mn}^{(1)}$ of the first layer into Eq. (6), the unknown coefficient matrix $XH_{mn}^{(i)}$ for any arbitrary i-th layer can be obtained. Finally, by substituting the coefficient matrix $XH_{mn}^{(i)}$ back into Eq. (2), the temperature at any position within the laminated plate can be determined, which represents the temperature distribution of the laminated plate. Once the coefficients are known, the temperature field for any layer is reconstructible.

In the local Cartesian coordinate system, the 3D thermoelastic constitutive equation for the i-th layer structure is as follows:

$$\begin{cases} \sigma_x^{(i)}(x,y,\bar{z}) = (\lambda^{(i)}+2G^{(i)})\frac{\partial u^{(i)}(x,y,\bar{z})}{\partial x} + \lambda^{(i)}\frac{\partial v^{(i)}(x,y,\bar{z})}{\partial y} + \lambda^{(i)}\frac{\partial w^{(i)}(x,y,\bar{z})}{\partial \bar{z}} - (3\lambda^{(i)}+2G^{(i)})\alpha^{(i)}T^{(i)}(x,y,\bar{z}), \\ \sigma_y^{(i)}(x,y,\bar{z}) = (\lambda^{(i)}+2G^{(i)})\frac{\partial v^{(i)}(x,y,\bar{z})}{\partial y} + \lambda^{(i)}\frac{\partial u^{(i)}(x,y,\bar{z})}{\partial x} + \lambda^{(i)}\frac{\partial w^{(i)}(x,y,\bar{z})}{\partial \bar{z}} - (3\lambda^{(i)}+2G^{(i)})\alpha^{(i)}T^{(i)}(x,y,\bar{z}), \\ \sigma_{\bar{z}}^{(i)}(x,y,\bar{z}) = (\lambda^{(i)}+2G^{(i)})\frac{\partial w^{(i)}(x,y,\bar{z})}{\partial \bar{z}} + \lambda^{(i)}\frac{\partial u^{(i)}(x,y,\bar{z})}{\partial x} + \lambda^{(i)}\frac{\partial v^{(i)}(x,y,\bar{z})}{\partial y} - (3\lambda^{(i)}+2G^{(i)})\alpha^{(i)}T^{(i)}(x,y,\bar{z}), \\ \tau_{xy}^{(i)}(x,y,\bar{z}) = G^{(i)}\left(\frac{\partial u^{(i)}(x,y,\bar{z})}{\partial y} + \frac{\partial v^{(i)}(x,y,\bar{z})}{\partial x}\right), \\ \tau_{y\bar{z}}^{(i)}(x,y,\bar{z}) = G^{(i)}\left(\frac{\partial v^{(i)}(x,y,\bar{z})}{\partial \bar{z}} + \frac{\partial w^{(i)}(x,y,\bar{z})}{\partial y}\right), \\ \tau_{x\bar{z}}^{(i)}(x,y,\bar{z}) = G^{(i)}\left(\frac{\partial u^{(i)}(x,y,\bar{z})}{\partial \bar{z}} + \frac{\partial w^{(i)}(x,y,\bar{z})}{\partial x}\right) \end{cases} \tag{6}$$

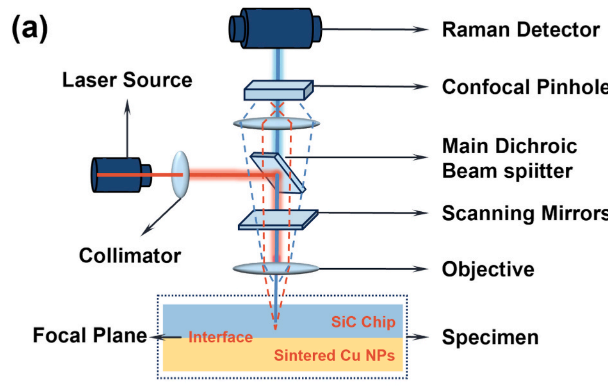

Fig. 3. Confocal Raman spectroscopy system: (a) Schematic diagram of confocal Raman spectroscopy system; (b) LabRAM Odyssey of HORIBA Scientific.

Here $\sigma_x^{(i)}(x,y,\bar{z})$, $\sigma_y^{(i)}(x,y,\bar{z})$, and $\sigma_{\bar{z}}^{(i)}(x,y,\bar{z})$ are the normal stresses in the x , y, and $\bar{z}$ directions of the i-th layer structure, respectively; $\tau_{xy}^{(i)}(x,y,\bar{z})$, $\tau_{y\bar{z}}^{(i)}(x,y,\bar{z})$, and $\tau_{x\bar{z}}^{(i)}(x,y,\bar{z})$ are the shear stresses of the i-th layer structure; and $u^{(i)}(x,y,\bar{z})$, $v^{(i)}(x,y,\bar{z})$, and $w^{(i)}(x,y,\bar{z})$ are the displacements in the x, y, and $\bar{z}$ directions of the i-th layer structure, respectively. Additionally, $G^{(i)}$ is the shear modulus, and $\lambda^{(i)}$ is the Lame constant, which can be expressed in terms of Young's modulus $E^{(i)}$ and Poisson's ratio $\mu^{(i)}$.

Subsequently, three differential equations concerning $U_{mn}^{(i)}(\bar{z})$, $V_{mn}^{(i)}(\bar{z})$, and $W_{mn}^{(i)}(\bar{z})$ can be derived. Subsequently, by solving these differential equations, the displacement field of the i-th layer structure is obtained and rewritten in the following matrix form:

$$\begin{bmatrix} u^{(i)}(x,y,\bar{z}) \\ v^{(i)}(x,y,\bar{z}) \\ w^{(i)}(x,y,\bar{z}) \end{bmatrix} = \sum_{m=1}^{\infty}\sum_{n=1}^{\infty}\left\{\left[\boldsymbol{DU}_{mn}^{(i)}\right]_{3\times 6}\left[\boldsymbol{XD}_{mn}^{(i)}\right]_{6\times 1} + \left[\boldsymbol{DH}_{mn}^{(i)}\right]_3\left[\boldsymbol{XH}_{mn}^{(i)}\right]_{2\times 1}\right\} \odot \begin{bmatrix} \cos\frac{m\pi x}{a}\sin\frac{n\pi y}{b} \\ \sin\frac{m\pi x}{a}\cos\frac{n\pi y}{b} \\ \sin\frac{m\pi x}{a}\sin\frac{n\pi y}{b} \end{bmatrix} \tag{7}$$

Here $\odot$ represents the Hadamard product. $DU_{mn}^{(i)}$ is a 3×6 matrix, $DH_{mn}^{(i)}$ is a 3×2 matrix, and $XH_{mn}^{(i)}$ is the aforementioned matrix of unknown coefficients for the temperature field. $XD_{mn}^{(i)}$ is a matrix of unknown

coefficients for the displacement field, determined by the stress boundary conditions and displacement boundary conditions. Subsequently, based on the continuity conditions at the interfaces, the corresponding matrix expressions are derived, allowing the six unknowns to be recursively determined.

A continuity of displacement and stress exists between the contact interfaces of adjacent layers in the laminated plate, and the displacement and stress on the upper surface of the i-th layer plate should be equal to the displacement and stress on the lower surface of the $(i+1)$-th layer plate.

Based on the continuity conditions between the mentioned laminated plates and using the matrix transmission method, the relationship between the displacement and stress on the upper surface of the i-th layer ($i = 1, 2, \ldots, p$) and the lower surface of the first layer can be obtained as follows:

$$\begin{cases} \boldsymbol{Y}_{mn}^{(i)}\left(h^{(i)}\right) = \prod_{i=p}^{1}\boldsymbol{D}_{mn}^{(i)}\left(h^{(i)}\right)\boldsymbol{D}_{mn}^{(i)}(0)^{-1}\boldsymbol{Y}_{mn}^{(1)}(0) + [\boldsymbol{S}_{mn}]_{6\times 1}, \\ \boldsymbol{S}_{mn} = -\sum_{j=1}^{p}\left\{\prod_{i=p}^{j}\left[\boldsymbol{D}_{mn}^{(i)}\left(h^{(i)}\right)\boldsymbol{D}_{mn}^{(i)}(0)^{-1}\right]\right\}\boldsymbol{B}_{mn}^{(j)}(0) + \sum_{j=2}^{p}\left\{\prod_{i=p}^{j}\left[\boldsymbol{D}_{mn}^{(i)}\left(h^{(i)}\right)\boldsymbol{D}_{mn}^{(i)}(0)^{-1}\right]\right\}\boldsymbol{B}_{mn}^{(j-1)}\left(h^{(j-1)}\right) + \boldsymbol{B}_{mn}^{(p)}(h^{(p)}) \end{cases} \tag{8}$$

Subsequently, mechanical loads are applied to the bottom surface of the laminated plate. Therefore, the additional boundary conditions for applying mechanical loads to the upper and lower surfaces of the laminated plate are as follows:

$$\begin{cases} \sigma_{\bar{z}}^{(1)}(x,y,0) = q(x,y), \\ \sigma_{\bar{z}}^{(p)}\left(x,y,h_p\right) = 0, \\ \tau_{x\bar{z}}^{(1)}(x,y,0) = 0, \\ \tau_{y\bar{z}}^{(1)}(x,y,0) = 0, \\ \tau_{x\bar{z}}^{(p)}(x,y,h^{(p)}) = 0, \\ \tau_{y\bar{z}}^{(p)}(x,y,h^{(p)}) = 0 \end{cases} \tag{9}$$

Here $q(x, y)$ represents the mechanical load applied to the bottom surface of the laminated plate. By substituting Eq. (8) into Eq. (9), the relationship between the displacement and stress on the bottom and top surfaces of the laminated plate is obtained as follows:

$$\boldsymbol{XD}_{mn}^{(i)} = \boldsymbol{D}_{mn}^{(i)}\left(h^{(i)}\right)^{-1}\left\{\prod_{i=p}^{1}\boldsymbol{D}_{mn}^{(i)}\left(h^{(i)}\right)\boldsymbol{D}_{mn}^{(i)}(0)^{-1}\begin{bmatrix} U_{mn}^{(1)}(0) \\ V_{mn}^{(1)}(0) \\ W_{mn}^{(1)}(0) \\ \frac{4}{ab}\int_0^b\int_0^a q(x,y)\sin\frac{m\pi x}{a}\sin\frac{n\pi y}{b}dxdy \\ 0 \\ 0 \end{bmatrix} + \boldsymbol{S}_{mn} - \boldsymbol{B}_{mn}^{(i)}\left(h^{(i)}\right)\right\} \tag{10}$$

By recursively operating on Eq. (10) based on the interface continuity conditions of the model, the coefficient matrix $XD_{mn}^{(i)}$ can be solved. Finally, by substituting the obtained coefficient matrix into Eq. (7), the triaxial displacement and stress components at any position within the laminated plate model under the combined action of mechanical and thermal loads can be determined. All the derivation and calculation processes are solved through logical programming in MATLAB. This model facilitates efficient, mesh-free evaluation of multilayer thermal deformation and interfacial stress. Its validity and predictive accuracy have been corroborated by comparison with finite element simulations, as discussed in Sec. 3.1.

2.3. Confocal Raman-based interfacial stress characterization

To enable spatially resolved analysis of interfacial stress in the SiC/Sintered Cu NPs/AMB stack, a confocal Raman spectroscopy system was employed for in-plane residual stress characterization. As illustrated in Fig. 3, measurements were performed using the LabRAM Odyssey high-speed, high-resolution confocal Raman microscope developed by HORIBA Scientific. Compared to conventional Raman configurations, this system incorporates a continuously adjustable confocal pinhole and a high numerical aperture objective lens, which significantly enhance axial (Z-directional) depth resolution. The laser focal point can be precisely positioned near the bottom surface of the SiC chip, effectively minimizing scattering interference from upper layers and allowing acquisition of Raman signals in the vicinity of the SiC/sintered Cu interface [38]. This configuration is particularly suitable for detecting localized residual stress concentrations arising from thermal expansion mismatches.

The Raman spectroscopy setup employed a 532 nm excitation laser with a 40× objective lens, a laser power of 5 mW, and an acquisition time of 1 s per sampling point. Previous studies have established the peak fitting procedure and stress calibration coefficients for 4H-SiC, which were adopted in this work [36,39]. It has also been demonstrated that, under such laser power and acquisition conditions, the heating effect of the confocal laser on SiC chips is negligible, and does not affect the accuracy of residual stress evaluation [40].

Raman measurements on the 4H-SiC chip were conducted in a backscattering configuration, with the incident laser aligned along the [0001] crystallographic direction (Z-axis) [41]. During testing, the laser focus was axially adjusted via the confocal optics to a position near the bottom surface of the chip, adjacent to the Cu NP interconnect layer. This enhanced the signal specificity from the interfacial region while suppressing contributions from upper layers. To ensure accurate identification of spectral peak positions, the system was calibrated prior to data acquisition with respect to focal alignment and baseline correction [42]. In-plane stress analysis was carried out by point-by-point linear scanning across the backside of the SiC chip. The measurement points were spaced at fixed 320 μm intervals. At each location, sufficient signal accumulation time was used to maintain a high signal-to-noise ratio. This scanning approach enabled spatially resolved mapping of the residual stress distribution induced by the sintering and bonding process in the SiC/Sintered Cu NPs/AMB stack.

In crystalline semiconductors such as 4H-SiC, the Raman frequency of characteristic phonon modes is perturbed by mechanical stress through its effect on interatomic spacing. Particularly, the E_2(TO) mode exhibits high sensitivity to in-plane stress, making it suitable for quantitative stress analysis. Under general stress conditions, the frequency shift $\Delta\omega$ can be modeled as a function of principal strain components using deformation potential theory [36,43]:

$$\Delta\omega = a(\varepsilon_{xx} + \varepsilon_{yy}) + b\varepsilon_{zz} \pm c\sqrt{(\varepsilon_{xx} - \varepsilon_{yy})^2 + 4\varepsilon_{xy}^2} \tag{11}$$

Here a, b and c represent mode-specific deformation potential coefficients, and ε_{ij} denote the components of the strain tensor. In the stress prediction model of 4H-SiC, a_{E2} and b_{E2} are phonon deformation potential coefficients, which quantify the sensitivity of the E_2 (TO) Raman mode to different strain components. Specifically, a_{E2} primarily reflects the influence of in-plane stress on the Raman frequency shift, while b_{E2} captures the contribution from the normal stress. Coupling this expression with the generalized Hooke's law allows the shift to be reformulated in terms of the applied stress:

$$\begin{pmatrix} \varepsilon_{xx} \\ \varepsilon_{yy} \\ \varepsilon_{zz} \end{pmatrix} = \begin{pmatrix} s_{11} & s_{12} & s_{13} \\ s_{12} & s_{11} & s_{13} \\ s_{13} & s_{13} & s_{33} \end{pmatrix} \begin{pmatrix} \sigma_{xx} \\ \sigma_{yy} \\ \sigma_{zz} \end{pmatrix} \tag{12}$$

where s_{11}, s_{12} and s_{13} are components of the compliance tensor, representing the direct in-plane elastic response (s_{11}), the in-plane coupling effect (s_{12}), and the coupling between in-plane and out-of-plane stresses (s_{13}). Together, these parameters establish the quantitative link between external loading, lattice strain, and Raman peak shifts. Substituting this into the Raman–strain relation yields:

$$\Delta\omega = [a_{E_2}(s_{11} + s_{12}) + b_{E_2}s_{13}]\cdot(\sigma_{xx} + \sigma_{yy}) + bs_{33}\cdot\sigma_{zz} \tag{13}$$

Assuming an equibiaxial stress state confined to the SiC chip plane, with negligible contributions from out-of-plane and shear components, the relation simplifies to a linear stress–shift equation:

$$\Delta\omega_{E_2} = 2[a_{E_2}(s_{11} + s_{12}) + b_{E_2}s_{13}]\Delta\sigma \tag{14}$$

where the coefficients a_{E2} and b_{E2} are derived from phonon–strain interaction theory and validated against experimental calibration under uniaxial and biaxial stress states. The compliance parameters (s_{11}, s_{12} and s_{13}) are obtained by molecular dynamics (MD) simulations, in which the elastic constant tensor of 4H-SiC is computed across different temperatures and then inverted to yield the compliance tensor, from which the relevant components are extracted. The detailed methodology of the MD simulations and the phonon–strain theoretical framework can be found in prior studies [36,40]. The stress conversion coefficient used in this work allows direct calculation of in-plane residual stress from the measured Raman shift of the E_2(TO) mode under equibiaxial loading conditions.

$$\Delta\sigma\,(\text{MPa}) = -323\Delta\omega_{\text{obs}}\,(\text{cm}^{-1}) \tag{15}$$

2.4. Temperature-dependent warpage measurement

Temperature-dependent deformation behavior was evaluated using COMPACT-3 XL, an optical thermal deformation measurement (TDM) system incorporating the Projection Moiré technique. This method enables high-resolution, full-field displacement capture by projecting structured light patterns onto the sample surface and analyzing the resulting fringe modulations. The Projection Moiré system was performed using a noise threshold of 0.5 mm, a standard-mode Fourier filter (width 3 px), a Gaussian filter (kernel size 10%), and a sorting rule that orders data by rows and then columns (part tracking disabled). A dual-sided infrared heating assembly was employed to deliver spatially uniform and rapidly adjustable thermal input within a three-dimensional test volume. As the temperature increased, thermal expansion induced out-of-plane surface displacement, resulting in the formation of moiré fringes—alternating light and dark bands—due to the interference between projected and reflected patterns. Fringe evolution was recorded using a calibrated high-resolution imaging unit, enabling quantitative extraction of surface warpage and deformation. All experiments were conducted in a test chamber equipped with vibration suppression and controlled airflow shielding to minimize environmental interference. Temperature was incrementally elevated from ambient conditions to a maximum of 310°C, with a maximum heating rate of 1 °C/s. Sample deformation was monitored continuously at selected temperature intervals, and image data were post-processed to derive deformation contours. Operator safety protocols were strictly implemented throughout high-temperature operations.

3. Results and discussion

3.1. Analytical model verification

In the present thermo-mechanical model, both the warpage field and interfacial stress components are formulated using a double Fourier series expansion to analytically represent the spatial distributions across the multilayer structure. The analytical solution requires truncating the series to finite terms m and n in the X and Y-directions, respectively. The selection of these truncation orders directly affects the precision and stability of the solution, necessitating a systematic convergence assessment.

As shown in Fig. 4, the predicted maximum warpage and interfacial stress vary considerably when the expansion orders are below 20, indicating insufficient resolution to describe the thermo-mechanical response. While increasing the orders improves accuracy, a saturation behavior is observed beyond $m = n = 25$, where further terms result in changes below 1.5%. Notably, overly large orders increase symbolic manipulation complexity and computational cost without meaningful gains in solution fidelity, particularly for repeated evaluations in parametric studies. Therefore, adopting $m = n = 25$ ensures that the dominant deformation and interfacial stress features are well captured while keeping computational demands manageable. This truncation level offers a practical compromise between accuracy and efficiency, and is used throughout all subsequent analytical evaluations. The convergence analysis confirms that the closed-form solution achieves numerical stability and reliable spatial resolution within the modeling framework, forming the theoretical basis for later finite element validation.

To further verify the predictive accuracy of the analytical thermo-mechanical model, comparative analysis was conducted against finite element simulation results. The FEM simulations were performed in Ansys Mechanical, incorporating the same material properties and geometric parameters as provided in Table 1, and subjected to identical thermal loading conditions as the analytical model. Vertical displacement was extracted along the central line on the top surface of the SiC

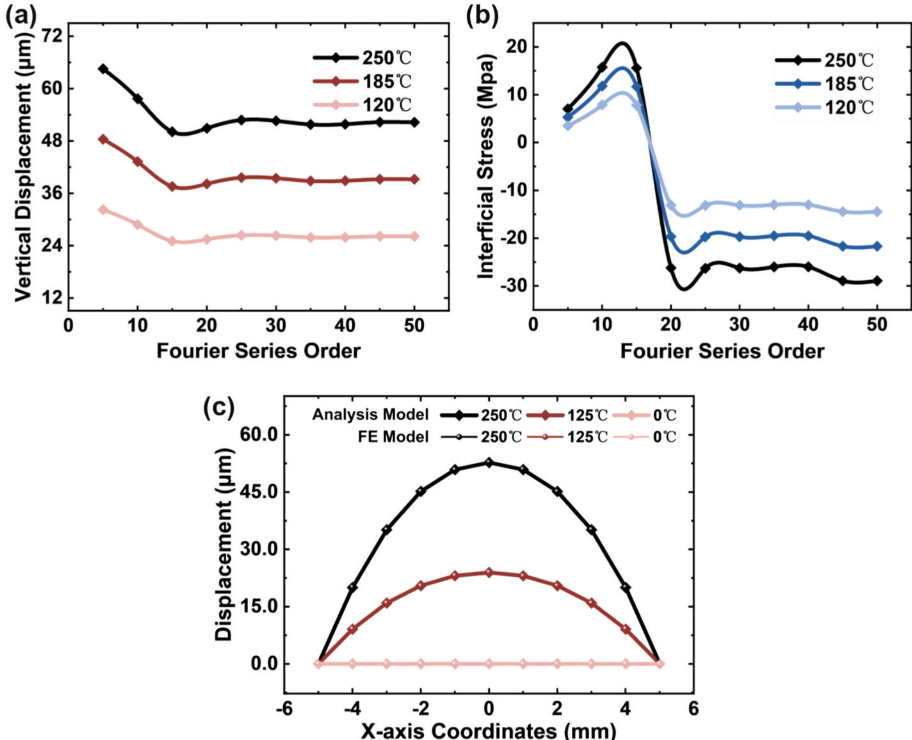

Fig. 4. Analytical model verification: (a) Convergence behavior of maximum vertical displacement with increasing Fourier series order under different temperature conditions; (b) Convergence of interfacial stress at the chip center as a function of Fourier truncation orders; (c) Model accuracy verification.

Table 1
Material properties and geometric parameters used in the analytical and FEM models for the SiC/Sintered Cu NPs/AMB stack [44–46].

Components	Materials	Thickness (mm)	K (W/m·°C)	CTE (ppm/°C)	E (GPa)	v
SiC Chip	SiC	0.36	58.6	5.1	400	0.14
Die-attachment	Sintered Cu NPs	0.02	390.0	17.3	13.2	0.34
AMB Substrate	Cu	0.1	401.0	18.0	110	0.34
	Si_3N_4	0.2	70.0	31.0	49	0.38
	Cu	0.1	401.0	18.0	110	0.34

chip at selected temperatures of 0°C, 125°C, and 250°C to represent critical thermo-mechanical responses.

As illustrated in Fig. 4(c), the predicted warpage profiles exhibit excellent agreement with FEM results across all evaluated conditions. The computed displacement curves closely follow the simulated ones, with a maximum relative deviation below 2%. Minor discrepancies, particularly at intermediate temperatures, are attributed to differences in boundary condition representation and discretization fidelity between the continuous analytical approach and the mesh-based finite element formulation.

In contrast to conventional FEM strategies that rely heavily on meshing, iterative solvers, and matrix operations, the present model is derived from closed-form thermo-mechanical principles using double Fourier series decomposition. This formulation enables rapid and reproducible predictions without suffering from meshing sensitivity or solution path dependencies. In addition, the model maintains numerical stability and physical consistency across a wide range of thermal conditions due to the controllable truncation strategy discussed previously. Notably, the proposed model retains high accuracy while offering orders-of-magnitude improvements in computational efficiency, particularly for parametric sweeps or design iterations. While FEM remains indispensable for highly complex or non-linear systems, this model demonstrates its utility as a lightweight alternative for high-throughput evaluations, early-stage package design, and educational modeling scenarios.

The demonstrated agreement with FEM validates the model's core assumptions and confirms its practical value in predicting warpage behavior in SiC/Sintered Cu NPs/AMB stacks. Its ability to capture the dominant thermally induced deformation features while maintaining low computational overhead establishes a promising framework for future analytical extensions and integration with multi-physics workflows.

3.2. Interfacial residual stress characterization

Fig. 5(a) presents the complete Raman spectrum of 4H-SiC, where the characteristic phonon peaks are clearly visible. This confirms the material identity and provides a reliable baseline for subsequent stress analysis. Fig. 5(b) shows the Raman spectra measured at different depths along the vertical direction of the SiC chip, spanning from the top surface toward the bottom. The characteristic peaks remain stable when the focal point is within the chip interior. Once the focal depth exceeds the full chip thickness of 360 μm, the peaks disappear, indicating that Raman signals can be stably and effectively acquired throughout the entire thickness of the 4H-SiC chip. Fig. 5(c) displays reference Raman spectra acquired from three spatially distributed positions along the SiC chip edge, including two symmetric locations near opposing corners and one point along the diagonal boundary. The E_2(TO) phonon peak for all three spectra consistently appears near 777 cm^{-1}, with negligible variation in peak position or shape. This spectral uniformity confirms that

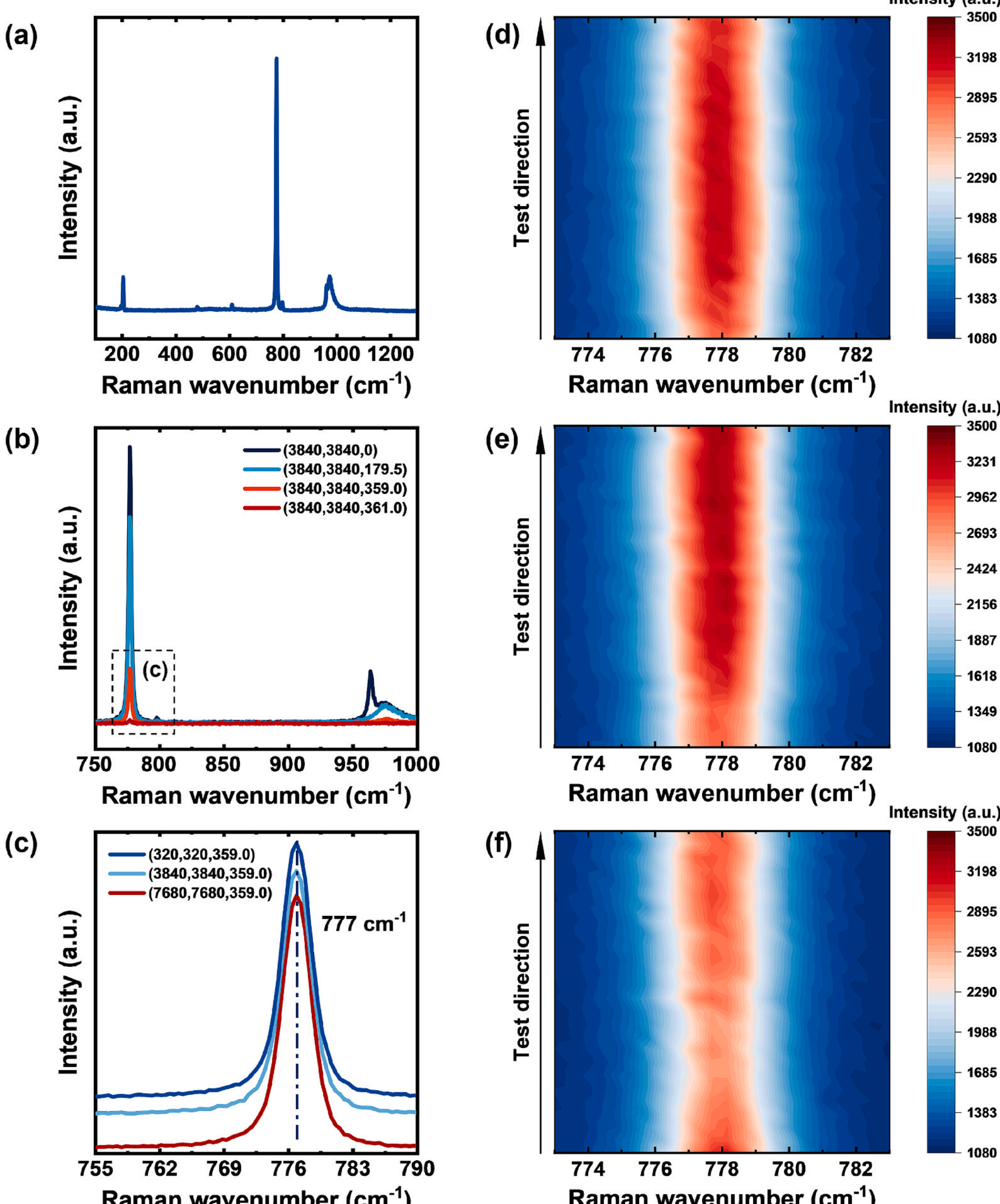

Fig. 5. Raman spectroscopy results and Raman peak-shift profiles for the SiC/Sintered Cu NPs/AMB stack. (a) Representative complete Raman spectra of 4H-SiC. (b) Raman spectra acquired at different depth. (c) Characteristic Raman peak measured on the backside of the un-sintered 4H-SiC chip. (d) Raman peak shift distributions of the SiC/Sintered Cu NPs/AMB stack at X= 320 μm. (e) Raman peak shift distributions at X= 2220 μm. (f) Raman peak shift distributions at X= 3840 μm.

these peripheral regions can be considered effectively stress-free, thus providing a stable baseline for subsequent peak shift analysis.

Fig. 5(d–f) display the position-resolved Raman peak shift profiles along three vertical sections located at X = 320 μm, X = 2220 μm, and X= 3840 μm, spanning from the bottom to the top edge of the bonded chip. In each section, the spectral peak demonstrates a redshift trend as the measurement point moves toward the geometric center of the chip along the Y-direction. Among the three line scans, the X= 3840 μm section—positioned closest to the physical center of the chip—exhibits the largest deviation in peak position, indicating the most stress response. The degree of spectral shift becomes progressively weaker in sections farther from the chip center, such as in the X = 320 μm scan, where the shift magnitude is notably lower and the spectral contours more symmetric. This spatial evolution in Raman response demonstrates a clear position-dependent trend, which suggests the presence of non-uniform residual mechanical effects localized near the chip center. These observations are consistent across all vertical sections and form the empirical basis for the subsequent stress mapping analysis presented in the next subsection.

In Fig. 6(a–b), the un-sintered 4H-SiC chip exhibits low residual-stress levels: the top surface ranges from −42.3 to 52.2 MPa, while the bottom surface shows tensile stresses ranging from 11.3 to 89.6 MPa. In Fig. 6(c–d), after bonding in the SiC/Sintered Cu NPs/AMB stack, the chip top surface displays tensile stresses ranging from 90.3 to 171.2 MPa, whereas the chip bottom surface (interface) shows compressive stresses ranging from −334.0 to −243.0 MPa. Both surfaces manifest a center-peaked pattern with attenuation toward the edges. This behavior is consistent with the Raman peak-shift profiles in Fig. 5 and corroborates an in-plane non-uniform residual field.

As illustrated in Fig. 6(c–d), the tensile field at the top surface and the compressive field at the bottom surface are mutually consistent, both peaking at the center. This agrees with the peak-shift profiles in Fig. 5

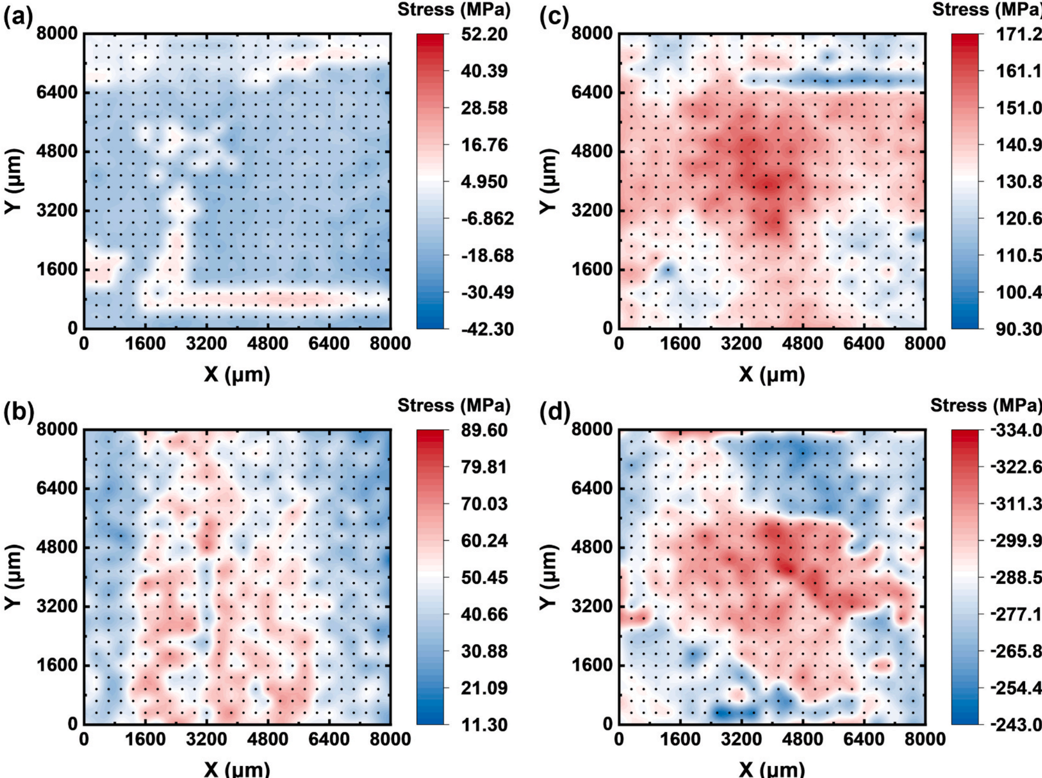

Fig. 6. Residual stress distribution obtained from Raman-based stress mapping: (a) Un-sintered chip, top surface; (b) Un-sintered chip, backside; (c) Post-sintered SiC/sintered-Cu/AMB assembly, chip top surface; (d) Post-sintered SiC/sintered-Cu/AMB assembly, chip backside.

and corroborates the in-plane non-uniformity of residual stresses. The measured distribution of compressive residual stress at the SiC/Sintered Cu NPs/AMB interface can be primarily attributed to the mismatch in CTEs among the constituent materials. During the pressure-assisted sintering process, the stack was subjected to a peak bonding temperature of 250°C. As the assembly cooled down to ambient conditions, differential contraction occurred due to the dissimilar CTEs, 5.1 × 10^{-6} K^{-1} for SiC and 17.3 × 10^{-6} K^{-1} for sintered Cu NPs. This mismatch leads to mechanical incompatibility, particularly at the rigidly bonded interface, where the constraint imposed by the surrounding structure inhibits free deformation. Because the silicon carbide chip exhibits a significantly lower CTE, it experiences a net tensile tendency upon cooling, whereas the copper layer undergoes more substantial contraction. However, due to the intimate mechanical bonding formed during sintering, these incompatible deformations are redistributed across the interface, inducing compressive stress within the SiC side, particularly near the chip bottom. This stress is not relaxed post-process, and remains embedded in the structure as a residual stress field. Furthermore, the observed spatial distribution featured peak stress near the chip center and attenuation toward the periphery, stems from geometric and mechanical symmetry. The central area of the chip is most constrained by surrounding material and substrate interactions, which suppresses deformation recovery and concentrates the compressive field. In contrast, the chip edges are more susceptible to out-of-plane relaxation, allowing partial release of mismatch-induced strain energy.

Beyond the global trend, Fig. 6(c–d) reveals localized hot spots along the edges and at several off-center locations. Two mechanisms are plausible. First, the un-sintered chip carries fabrication-induced pre-stresses from thinning, laser dicing, and metallization, which can seed local variability; however, their magnitudes are far below the post-sinter interfacial concentrations (−334.0 to −243.0 MPa). Second, sintered Cu NP interconnects exhibit microstructural porosity and sintering-neck morphology [6]. Under pressure-assisted sintering, these features can induce interfacial discontinuities in stress transfer [47], generating localized compressive concentrations at the bonded interface in the SiC/Sintered Cu NPs/AMB stack.

In summary, the residual-stress field in the SiC/Sintered Cu NPs/AMB stack arises from the superposition of the mismatch in CTEs, chip pre-stress and microstructure-driven interfacial non-uniformity, yielding a state that is globally center-concentrated yet locally heterogeneous.

3.3. Model correction and validation

To incorporate the influence of residual stress introduced by the die-attach process, the original thermo-mechanical model was revised by adjusting the temperature boundary conditions. Specifically, both the upper and lower surfaces of the stack (T_u and T_b) were set to the sintering temperature (250°C), rather than ambient temperature. This correction assumes the bonded interface enters a stress-free state only at the process temperature where metallurgical bonding occurs, embedding the residual field induced by subsequent cooling into the model.

The impact of this correction was further validated through temperature-dependent warpage measurements using the projection moiré technique. As illustrated in Fig. 7(a), the sample underwent a controlled thermal cycle between 30°C and 310°C, with consistent heating and cooling rates. Fig. 7(b) shows the measured warpage evolution of the AMB substrate's underside, while Fig. 7(c) presents the chip's top surface deformation at each temperature point. The measured trend reveals a distinct thermoelastic behavior: maximum warpage occurs at room temperature, progressively decreasing as the temperature approaches 250°C, where the structure flattens to a near-zero curvature state. Upon further heating beyond the sintering point, the warpage reverses direction, indicating a mechanical polarity flip in thermal mismatch. During cooling, the warpage curve retraces in reverse, confirming a reversible deformation path. The relative warpage amplitude

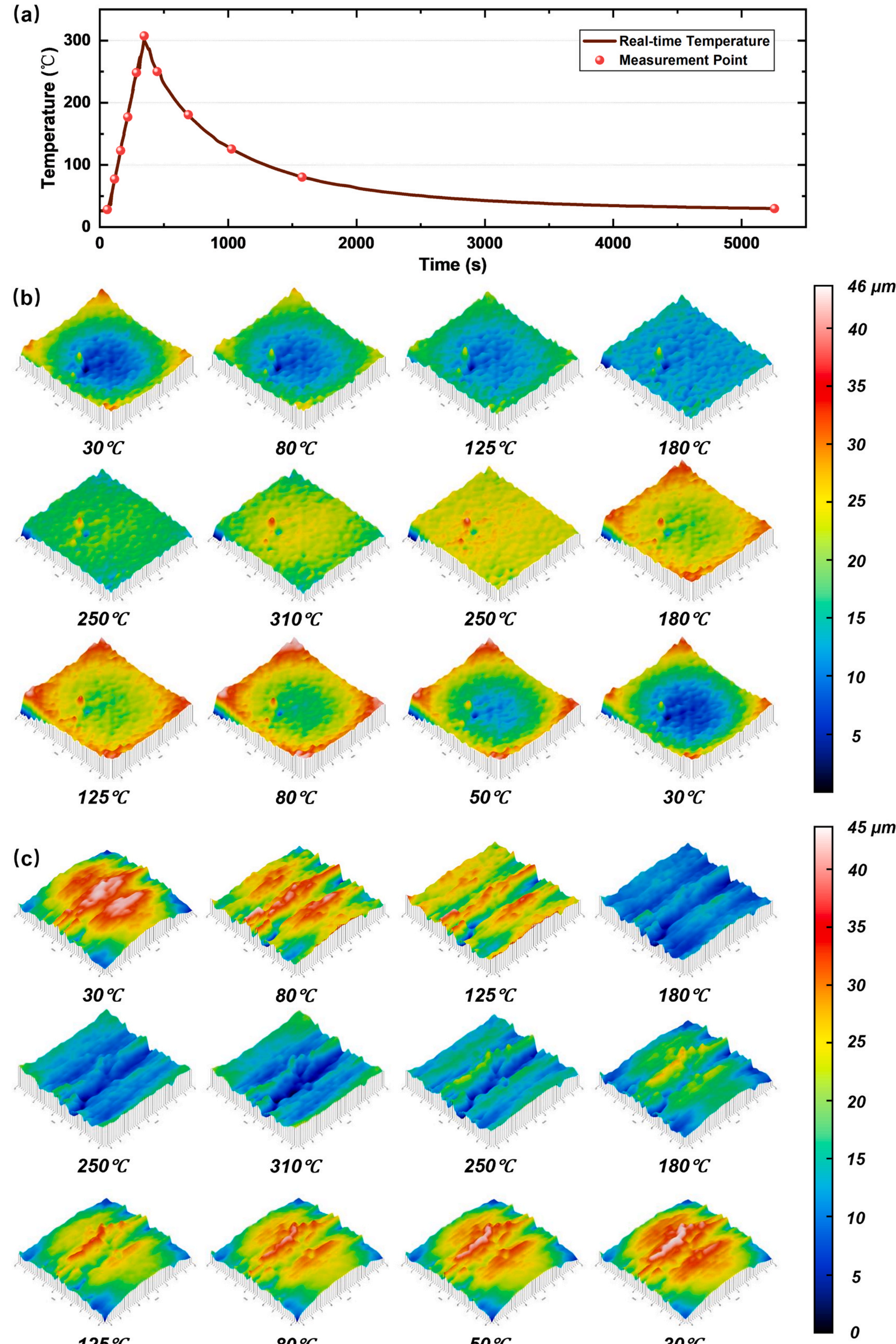

Fig. 7. Temperature-dependent warpage measurement of the SiC/Sintered Cu NPs/AMB stack: (a) Temperature evolution curve during heating and cooling; (b) Warpage distribution of the AMB substrate backside; (c) Warpage distribution of the SiC chip top surface.

Fig. 8. Comparison of experimental results, uncorrected model, and corrected model results for different thermal states before and after model correction: (a) 30°C, (b) 180°C, (c) 250°C, (d) 310°C, (e) 250°C (cooling), (f) 180°C (cooling), (g) 30°C (cooling).

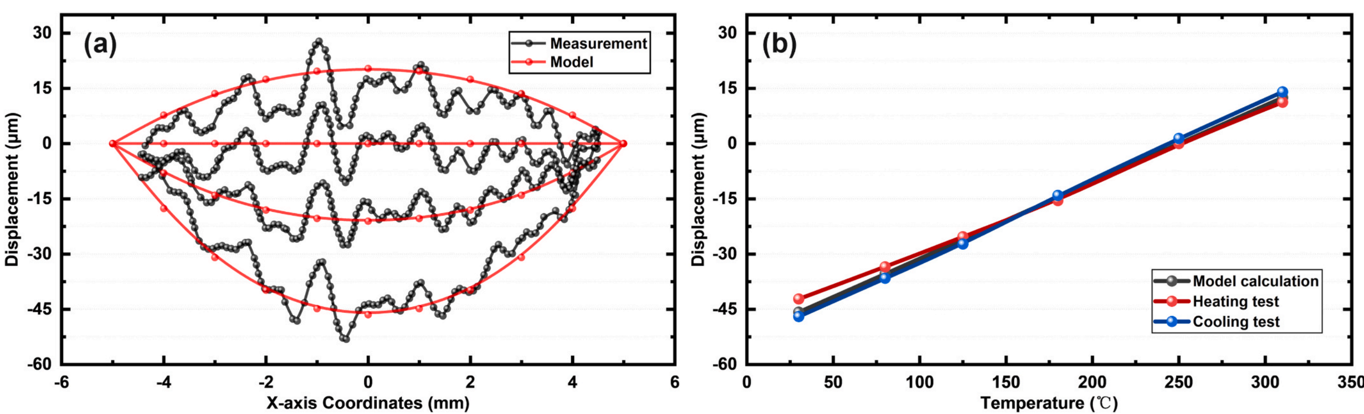

Fig. 9. Accuracy assessment of the corrected model under different thermal loading conditions: (a) Predicted warpage profiles at multiple temperature points; (b) Relative error curves of model prediction versus experiment during heating and cooling.

spans approximately 0 to 25 μm, highlighting the high sensitivity of the stack geometry to thermal loading and interfacial constraint. In summary, the presence of process-induced residual stress fundamentally alters the thermo-mechanical trajectory of the SiC/Sintered Cu NPs/AMB structure during a temperature cycle: without residual stress, the stack would evolve from an initially flat state → center-up warpage →

back to flat; when residual stress is included, the sequence becomes warped (as-bonded) → partial recovery → opposite-sign warpage → recovery → re-warpage.

These observations confirm that omitting residual stress in the model leads to systematic errors, especially in the low-to-intermediate temperature regime. The correction thus forms the necessary foundation for accurate thermal deformation prediction in such strongly bonded, multilayer packaging structures.

The predictive accuracy of the corrected model was evaluated against full-field experimental warpage data across a representative thermal cycle. As shown in Fig. 8, the chip's out-of-plane displacement was measured at seven key temperature points: 30°C, 180°C, 250°C, 310°C, and the corresponding cooling steps back to 250°C, 180°C and 30°C. Experimental results were compared with both the original model, which excluded residual stress, and the revised formulation incorporating the die-attach bonding temperature as the stress-free reference. The original model failed to capture the correct deformation pattern. It predicted reversed curvature trends and showed substantial deviation in magnitude, especially during heating and cooling transitions. By contrast, the corrected model—anchored at 250°C to reflect the bonding-induced residual stress—aligned closely with experimental observations at all temperature points.

Fig. 9 summarizes the relative error between model predictions and experimental data at the location of peak warpage. The relative error is defined using the maximum warpage displacement as the metric, computed as the ratio between the absolute difference of the corrected-model prediction and the experimental measurement and the experimental value. Across both heating and cooling phases, the corrected model consistently maintained deviations within 5%, demonstrating strong agreement with measured responses.

The proposed Raman–model coupled framework captures this shift by explicitly seeding the initial interfacial stress field measured by confocal Raman into the analytical prediction, thereby yielding more realistic warpage evolution under thermal cycling. Because this workflow disentangles the initial residual stress from the subsequent temperature-driven response, it is directly transferable to other interconnect systems (e.g., Ag-NP sinters, Sn-based solders, or alternative AMB ceramics), where manufacturing histories likewise imprint interfacial stress fields. Moreover, the quantified residual stress and its temperature dependence provide inputs and measurable baselines for assessing long-term concerns, such as cyclic ratcheting, low-cycle fatigue, and interfacial delamination.

While the analytical model closely matches the measured thermal warpage, it relies on idealized assumptions—perfect bonding, linear elasticity, and isotropy. Given the inherent porosity and microstructural anisotropy of sintered Cu NP interconnects, local stress and warpage may deviate from these idealizations. The current framework delivers a practical apparent prediction at the package scale, yet it abstracts away microstructural details. Future work will relax these assumptions by embedding porosity- and anisotropy-aware constitutive laws and interfacial imperfection to improve realism.

These results confirm that incorporating residual stress is essential for capturing the true thermo-mechanical behavior of SiC/Sintered Cu NPs/AMB stacks. The corrected model not only reproduces the observed warpage trends but also achieves high quantitative accuracy, making it a reliable tool for thermal reliability assessment in advanced power packaging.

4. Conclusion

This study establishes a high-fidelity modeling and optical characterization framework for evaluating the thermo-mechanical performance of SiC/Sintered Cu NPs/AMB stacks in power electronic packaging. The proposed methodology enables both accurate physical insight and scalable predictive capability. These findings provide theoretical foundation and diagnostic strategies for the design and reliability assessment of advanced interconnect structures, offering strong potential for engineering application and academic advancement. The key conclusions are summarized as follows:

(a) Confocal Raman spectroscopy was innovatively employed at the packaging scale to spatially resolve interfacial residual stress. A peak compressive stress of approximately −336 MPa was detected at the SiC/Cu interface, concentrated near the chip center. The residual-stress field in the SiC/Sintered Cu NPs/AMB stack arises from the superposition of the mismatch in CTEs, chip prestress and microstructure-driven interfacial non-uniformity, yielding a state that is globally center-concentrated yet locally heterogeneous.

(b) A fully analytical thermo-mechanical model based on thermoelastic theory and double Fourier series expansion was constructed. The model exhibits excellent convergence behavior at $m = n = 25$ and achieves prediction accuracy within 2% of FEM results, significantly reducing computational cost while preserving fidelity.

(c) Thermal warpage testing revealed that the structure exhibits maximum curvature at room temperature, gradually flattens with heating, and reverses warpage direction beyond the sintering temperature (250°C). This behavior reflects the release and redistribution of residual stress under varying thermal loads.

(d) By resetting the model's initial condition to the sintering temperature, residual stress effects were incorporated into the model. The corrected simulation accurately reproduced experimental warpage trends across heating and cooling stages, with relative errors consistently maintained below 5 %.

Future work should relax the assumptions of perfect bonding and isotropic elasticity by incorporating microstructural porosity and anisotropy of sintered Cu NPs, to further enhance predictive fidelity.

Declaration of competing interest

The authors declare that they have no known competing financial interests or personal relationships that could have appeared to influence the work reported in this paper.

Acknowledgements

The work described in this paper was supported by the National Natural Science Foundation of China (Grant No. 52275559), China Scholarship Council (Grant No. 202406100064) and Shanghai SiC Power Devices Engineering & Technology Research Center (Grant No. 19DZ2253400).

Data availability

Data will be made available on request.

References

[1] C.R. Eddy, D.K. Gaskill, Silicon carbide as a platform for power electronics, Science 324 (5933) (2009) 1398–1400, https://doi.org/10.1126/science.1168704.
[2] M.J. Tadjer, Toward gallium oxide power electronics Ultrawide-bandgap semiconductors show promise for high-power transistors, Science 378 (6621) (2022) 724–725, https://doi.org/10.1126/science.add2713.
[3] M. Abtew, G. Selvaduray, Lead-free solders in microelectronics, Mater. Sci. Eng. R-Rep. 27 (5–6) (2000) 95–141, https://doi.org/10.1016/S0927-796X(00)00010-3.
[4] C.T. Chen, S.J. Nagao, K. Suganuma, J.T. Jiu, T. Sugahara, H. Zhang, T. Iwashige, K. Sugiura, K. Tsuruta, Macroscale and microscale fracture toughness of microporous sintered Ag for applications in power electronic devices, Acta Mater. 129 (2017) 41–51, https://doi.org/10.1016/j.actamat.2017.02.065.
[5] Y.J. Wang, D. Xu, H.D. Yan, C.F. Li, C.T. Chen, W.L. Li, Low-temperature copper sinter-joining technology for power electronics packaging: a review, J. Mater. Process. Technol. 332 (2024), https://doi.org/10.1016/j.jmatprotec.2024.118526.

[6] L.M. Du, K. Liu, D. Hu, O. Bäcke, X. Hu, X.R. Ji, J.J. Fan, R.H. Poelma, M. H. Colliander, G.Q. Zhang, Microstructural and mechanical anisotropy in pressure-assisted sintered copper nanoparticles, Acta Mater. 287 (2025), https://doi.org/10.1016/j.actamat.2025.120772.
[7] W.W. Zhang, P.H. Zhang, D.S. Lu, H. Pan, X.L. Liu, C.Y. Xu, J. Wei, M.Y. Li, H.J. Ji, A supersaturated Cu-Ag nanoalloy joint with ultrahigh shear strength and ultrafine nanoprecipitates for power electronic packaging, J. Mater. Sci. Technol. 145 (2023) 56–65, https://doi.org/10.1016/j.jmst.2022.10.038.
[8] Z.Y. Li, H.L. Luo, Y.G. Jiang, H.C. Liu, L. Xu, K.Y. Cao, H.J. Wu, P. Gao, H. Liu, Comprehensive review and future prospects on chip-scale thermal management: Core of data center's thermal management, Appl. Therm. Eng. 251 (2024), https://doi.org/10.1016/j.applthermaleng.2024.123612.
[9] J.H. Yan, Z.Y. Liu, Z.J. Liu, Y.J. Wang, D. Wang, L.M. Shen, A performance degradation and lifetime prediction model for thermoelectric device under thermal cycling, Appl. Therm. Eng. 274 (2025), https://doi.org/10.1016/j.applthermaleng.2025.126655.
[10] Y.K. Wang, H.Z. Liu, L.H. Huo, H.B. Li, W.C. Tian, H.Y. Ji, S. Chen, Research on the reliability of advanced packaging under multi-field coupling: a review, Micromachines 15 (4) (2024), https://doi.org/10.3390/mi15040422.
[11] X.M. Zhou, Y.C. Liu, M. Ali, M. He, A multilevel-multiphysics modeling and simulation approach for multichip electronics, Appl. Therm. Eng. 266 (2025), https://doi.org/10.1016/j.applthermaleng.2025.125738.
[12] C. Wang, M.J. Qiu, Z.K. Pan, K.Y. Zhou, T. Wang, J. Hong, Q.Y. Lin, Optimized design of contact interfaces for enhanced heat dissipation in flip-chip package, Appl. Therm. Eng. 259 (2025), https://doi.org/10.1016/j.applthermaleng.2024.124936.
[13] F.Z. Hou, T.Y. Lin, L.Q. Cao, F.M. Liu, J. Li, X.J. Fan, G.Q. Zhang, Experimental verification and optimization analysis of warpage for panel-level fan-out package, IEEE Trans. Compon. Packag. Manuf. Technol. 7 (10) (2017) 1721–1728, https://doi.org/10.1109/tcpmt.2017.2726084.
[14] X. Yan, W. Chen, W. Li, J. Jiang, X. Fan, G. Zhang, J. Fan, Multi-Objective Optimization of a 1200-V Fan-Out Panel-Level SiC MOSFET Packaging with Improved Genetic and Particle Swarm Algorithms, in: 2024 IEEE 74th Electronic Components and Technology Conference (ECTC), IEEE, 2024, pp. 2143–2149.
[15] J.H. Wong, N. Wu, W.H. Lai, D.L. Chen, T.Y. Chen, C.H. Chen, Y.H. Wu, Y.S. Chang, C.L. Kao, D. Tarng, T.C. Lee, Warpage and RDL stress analysis in large fan-out package with multi-chiplet integration, in: 2022 IEEE 72nd Electronic Components and Technology Conference (ECTC), IEEE, 2022, pp. 1074–1079.
[16] M. Alabdali, F.M. Zanotto, M. Chouchane, A.C. Ngandjong, V. Viallet, V. Seznec, Y. S. Meng, A.A. Franco, Understanding mechanical stresses upon solid-state battery electrode cycling using discrete element method, Energy Storage Mater. 70 (2024), https://doi.org/10.1016/j.ensm.2024.103527.
[17] Q.H. Nguyen, L.B. Nguyen, H.B. Nguyen, H. Nguyen-Xuan, A three -variable high order shear deformation theory for isogeometric free vibration, buckling and instability analysis of FG porous plates reinforced by graphene platelets, Compos. Struct. 245 (2020), https://doi.org/10.1016/j.compstruct.2020.112321.
[18] Z. Zhang, D. Zhou, H. Fang, J.D. Zhang, X.H. Li, Analysis of layered rectangular plates under thermo-mechanical loads considering temperature-dependent material properties, App. Math. Model. 92 (2021) 244–260, https://doi.org/10.1016/j.apm.2020.10.036.
[19] R. Sattari, D. Hu, X. Liu, H. van Zeijl, S. Vollebregt, G.Q. Zhang, Transient thermal measurement on nano-metallic sintered die-attach joints using a thermal test chip, Appl. Therm. Eng. 221 (2023), https://doi.org/10.1016/j.applthermaleng.2022.119503.
[20] S. Xiang, G.W. Kang, Static analysis of functionally graded plates by the various shear deformation theory, Compos. Struct. 99 (2013) 224–230, https://doi.org/10.1016/j.compstruct.2012.11.021.
[21] X. Wu, Z. He, S. Zhao, X. Huang, Prediction and design of composite laminate with adjustable thermal expansion coefficient, Chinese J. Appl. Mech. 40 (3) (2023) 636–642.
[22] M.Y. Tsai, Y.W. Wang, A theoretical solution for thermal warpage of flip-chip packages, IEEE Trans. Compon. Packag. Manuf. Technol. 10 (1) (2020) 72–78, https://doi.org/10.1109/tcpmt.2019.2933546.
[23] X.L. Wang, X.Y. Yan, W.Y. Li, W. Du, L.F. Cai, G.W. Yang, Z.D. Wang, Z.Q. Wang, J. J. Fan, Thermal-induced warpage characterization for laminated packaging with three-dimensional thermoelasticity modeling and projection moiré measurement, Appl. Therm. Eng. 263 (2025), https://doi.org/10.1016/j.applthermaleng.2024.125324.
[24] P.J. Withers, H. Bhadeshia, Overview -: residual stress part 1 -: measurement techniques, Mater. Sci. Technol. 17 (4) (2001) 355–365, https://doi.org/10.1179/026708301101509980.
[25] J. Lu, Handbook of measurement of residual stresses, (No Title) (1996).
[26] H. Jiang, Y. Shen, T. Zhang, Residual Stress Evaluation of Multilayer Viscoelastic Composites Using Ultrasonic Acoustoelastic Effects, in: ASME International Mechanical Engineering Congress and Exposition, Vol. 87585, American Society of Mechanical Engineers, 2023 V001T01A020.
[27] A. Makino, D.V. Nelson, E.A. Fuch, D.R. Williams, Determination of biaxial residual stresses by a holographic-hole drilling technique, J. Eng. Mater. Technol.-Trans. ASME 118 (4) (1996) 583–588, https://doi.org/10.1115/1.2805960.
[28] M.E. Kartal, F.P.E. Dunne, A.J. Wilkinson, Determination of the complete microscale residual stress tensor at a subsurface carbide particle in a single-crystal superalloy from free-surface EBSD, Acta Mater. 60 (13–14) (2012) 5300–5310, https://doi.org/10.1016/j.actamat.2012.06.027.
[29] Y.Q. Zhang, L.M. Du, O. Bäcke, S. Kalbfleisch, G.Q. Zhang, S. Vollebregt, M. H. Colliander, Measuring residual stresses in individual on-chip interconnects using synchrotron nanodiffraction, Appl. Phys. Lett. 124 (8) (2024), https://doi.org/10.1063/5.0192672.
[30] F.F. Hu, T.Y. Qin, Y.H. Su, L.H. He, N. Ao, J.D. Parker, T. Shinohara, S.C. Wu, Residual stress relaxation of railway gradient S38C steel during fatigue crack growth by neutron imaging and diffraction, Int. J. Fatigue 193 (2025), https://doi.org/10.1016/j.ijfatigue.2025.108826.
[31] H.Y. Zhai, C.H. Liu, X.Q. Shang, H.M. Wang, M.H. Mathon, S.Y. Zhong, Measuring texture-component-dependent stress of CuZn39Pb2 by neutron diffraction, Int. J. Mech. Sci. 270 (2024), https://doi.org/10.1016/j.ijmecsci.2024.109109.
[32] X.U. Yongjian, L.U.O. Ronghui, G.U.O. Maotian, W.U. Junfu, L.I. Mingyu, The application and development of confocal Raman micro-spectroscopy, Laser J. 28 (2) (2007) 13–14.
[33] S. Román-Sánchez, A. Moure, A. del Campo, I. Lorite, J.F. Fernández, A. Serrano, Assessment of thermo-mechanical phenomena in Si-based diodes via operando confocal Raman microscopy, Measurement 229 (2024), https://doi.org/10.1016/j.measurement.2024.114425.
[34] Z. Stein, R. Naraparaju, U. Schulz, L. Tetard, S. Raghavan, Residual stress effects of CMAS infiltration in high temperature jet engine ceramic coatings captured non-destructively with confocal Raman-based 3D rendering, J. Eur. Ceram. Soc. 43 (4) (2023) 1579–1589, https://doi.org/10.1016/j.jeurceramsoc.2022.11.003.
[35] I.D. Breev, K.V. Likhachev, V.V. Yakovleva, R. Hübner, G.V. Astakhov, P. G. Baranov, E.N. Mokhov, A.N. Anisimov, Stress distribution at the AlN/SiC heterointerface probed by Raman spectroscopy, J. Appl. Phys. 129 (5) (2021), https://doi.org/10.1063/5.0029682.
[36] Z.D. Yang, X.Y. Wang, Y.H. Zuo, Z.R. Tang, B.T. Guo, J.R. Zhang, H.Y. Tang, R. J. Zhang, X.J. Fan, G.Q. Zhang, J.J. Fan, Prediction of temperature-dependent stress in 4H-SiC using in situ nondestructive raman spectroscopy characterization, Laser Photonics Rev. 19 (3) (2025), https://doi.org/10.1002/lpor.202401033.
[37] D. Hu, Z. Cui, J.J. Fan, X.J. Fan, G.Q. Zhang, Thermal kinetic and mechanical behaviors of pressure-assisted Cu nanoparticles sintering: a molecular dynamics study, Results Phys. 19 (2020), https://doi.org/10.1016/j.rinp.2020.103486.
[38] L.R. Qiu, H. Cui, Y. Wang, K.M. Xu, W.Q. Zhao, Research progress on high resolution laser differential confocal Raman spectroscopy, Acta Opt. Sin. 43 (15) (2023), https://doi.org/10.3788/aos230753.
[39] M. Yamaguchi, M. Fujitsuka, S. Ueno, I. Miura, W. Erikawa, T. Tomita, Study of indentation damage in single crystal silicon carbide by using micro Raman spectroscopy, in: Materials Science Forum, Vol. 645, Trans Tech Publications Ltd, 2010, pp. 551–554.
[40] Z.D. Yang, J. Tian, X.Y. Wang, J.W. Chen, Y.H. Zuo, R.J. Zhang, H.Y. Tang, X. J. Fan, G.Q. Zhang, J.J. Fan, Decoupling of nanoindentation residual stress field in single-crystalline 4H-SiC via micro-Raman spectroscopy, Opt. Lett. 50 (11) (2025) 3513–3516, https://doi.org/10.1364/OL.563213.
[41] I.D. Breev, A.V. Poshakinskiy, V.V. Yakovleva, S.S. Nagalyuk, E.N. Mokhov, R. Hübner, G.V. Astakhov, P.G. Baranov, A.N. Anisimov, Stress-controlled zero-field spin splitting in silicon carbide, Appl. Phys. Lett. 118 (8) (2021), https://doi.org/10.1063/5.0040936.
[42] M.D. Wang, Y. Liu, Y. Li, Q.B. Li, H.T. Li, M.Y. Wei, Y.F. Li, Y.M. Zong, X. Zhao, Three-dimensional (3D) nondestructive characterization of the spatial distribution and complex properties of polytypes on 4H-SiC wafers, ACS Appl. Electron. Mater. 6 (9) (2024) 6857–6867, https://doi.org/10.1021/acsaelm.4c01244.
[43] Q. Kang, X.D. Fang, C. Wu, H. Sun, Z.Y. Fang, B. Tian, L. Zhao, S.L. Wang, N. Zhu, P. Verma, M. Ryutaro, Z.D. Jiang, Improvement mechanism of brittle-plastic transition and residual stress in scratching 4H-SiC implanted by hydrogen ions, Ceram. Int. 48 (18) (2022) 27076–27087, https://doi.org/10.1016/j.ceramint.2022.06.019.
[44] D. Hu, C. Qian, X. Liu, L.M. Du, Z.C. Sun, X.J. Fan, G.Q. Zhang, J.J. Fan, High temperature viscoplastic deformation behavior of sintered nanocopper paste used in power electronics packaging: insights from constitutive and multi-scale modelling, J. Mater. Res. Technol.-JMR&T 26 (2023) 3183–3200, https://doi.org/10.1016/j.jmrt.2023.08.086.
[45] N. Nishiyama, S. Kitani, Y. Ohta, E. Kulik, Z. Netriová, A. Holzheid, Z. Lencés, H. Kawaji, F. Wakai, Low temperature heat capacity measurements of β-Si_3N_4 and γ-Si_3N_4: determination of the equilibrium phase boundary between β-Si_3N_4 and γ-Si_3N_4, J. Eur. Ceram. Soc. 40 (16) (2020) 6309–6315, https://doi.org/10.1016/j.jeurceramsoc.2019.11.025.
[46] L. Sementilli, D.M. Lukin, H.P. Lee, J.S. Yang, E. Romero, J. Vuckovic, W.P. Bowen, Low-dissipation nanomechanical devices from monocrystalline silicon carbide, Nano Lett. 25 (15) (2025) 6069–6075, https://doi.org/10.1021/acs.nanolett.4c06475.
[47] X.Y. Yan, L.M. Du, C. Gu, T.C. Tian, C.S. Gao, G.Q. Zhang, J.J. Fan, Microscale mechanical properties in sintered copper nanoparticles, Mater. Sci. Eng. A-Struct. Mater. Propert. Microstruct. Process. 943 (2025), https://doi.org/10.1016/j.msea.2025.148684.